

DRAFT

GT2025-153003

RELATING CUTOFF PRESSURE DISTRIBUTION AND ACOUSTIC SIGNATURE OF CENTRIFUGAL FANS THROUGH EXPERIMENTAL CORRELATION

Till M. Biedermann

TH Nürnberg Georg Simon Ohm
Nuremberg, Germany

Dennis Kammerzelt

TH Nürnberg Georg Simon Ohm
Nuremberg, Germany

ABSTRACT

Potential noise sources of rotating machinery are diverse and complex. This includes the acoustic signature of the impeller itself and the design of the fan casing. This is especially true for centrifugal fans with an asymmetric spiral casing. Here, a non-uniform and unsteady pressure field interacts with the volute cutoff, thus resulting in broadband noise radiation and, under given geometric circumstances, significant tonal noise effects. The current study investigates the relation between the local pressure distribution at the volute cutoff and the acoustic far-field signature of the fan. A low-speed centrifugal fan, placed in an anechoic environment, is equipped with pressure sensors to gather information on the mean pressure distribution and the unsteady wall pressure field at selected spots. Correlating the captured signature with the radiated far-field noise reveals significant common spectral components and helps identify relevant noise sources, affected by the volute cutoff. In the long term, the definition of transfer functions between the near-field wall pressure and the radiated noise into the far-field is expected to enhance the geometric optimisation of the volute cutoff in both experimental and numerical environments. The test rig, in close agreement with ISO 5801, allows for simultaneous capture of the aerodynamic performance, allowing for an analysis of the pressure correlation along the entire characteristic curve.

Keywords: Aeroacoustics, unsteady wall pressure, centrifugal fans, aerodynamics, experimental correlation

1. INTRODUCTION

A key factor in the interaction between the fan impeller and the fan volute is the position of the volute cutoff (tongue), which determines the direction of the flow, either exiting the volute or returning into it, thus affecting both the aerodynamic and acoustic performance [1-3]. The current investigation aims to analyse the local pressure distribution on the volute cutoff and relate it to the acoustic far-field radiation. This approach enables the fan designer to wisely choose the parameters of the volute

cutoff, preventing significant noise radiation through simple measures. Furthermore, gaining a better understanding of these effects opens up the potential for optimising fan performance simply by repositioning and/ or altering the cutoff design. Apart from the cutoff design per se, the distance between the cutoff and the impeller interacts with the optimum cutoff design parameters. Patil et al. [4] examined the effects of gradually reducing the distance between the impeller and the cutoff by modifying the entire spiral. Their results show a decrease in aerodynamic performance under design conditions, while under overload conditions, both efficiency and static pressure increase thorough altering the tip gap flows. The impact of tongue modifications on unsteady flow, pressure fluctuations, and noise radiation has been experimentally studied by Dong et al. [5]. A key finding is that an increasing gap between the tongue and impeller leads to irregular impeller outflow due to jet/wake interactions. A threshold of 20% of the impeller radius was found to significantly reduce tonal noise generation. For larger distances, minimal acoustic benefits were obtained while negatively affecting the aerodynamic performance. Neise et al. [2] provide an overview of various noise generation and reduction strategies for centrifugal fans, also considering the location and orientation of the volute cutoff and the volute casing. A related study focusing on the aeroacoustic effects of the volute cutoff is presented by Zhang et al. [6]. Their numerical simulations show that the primary noise peak of the centrifugal fan occurs at the blade passing frequency (BPF), with the source located near the volute cutoff. Manoochehr et al. [7] investigated tonal noise reduction techniques by developing tiered tongue elements designed to produce destructive interference at specific design frequencies, achieving promising results in reducing emitted noise.

In a subsequent study, Biedermann et al. [8] explored the aeroacoustic and aerodynamic effects of varying the position of a centrifugal impeller within a given spiral casing. This also includes changing the distance between the impeller and the

volute cutoff. Regarding aerodynamics, the minimum radii of the tested volute cutoff designs were advantageous. Aeroacoustically, high sensitivity to the distance between the impeller and the cutoff was observed, resulting in minimal noise radiation when high cutoff radii, larger distances between the cutoff and impeller, and lower positioning of the impeller within the casing were applied. The latter led to reduced inflow angles at the cutoff separation point.

Darwish. et al. [9] conducted a numerical study regarding the geometrical modifications of a low-pressure centrifugal drum-impeller (30 – 52 blades) and the volute cutoff to reduce the tonal noise. They numerically monitored the pressure distribution at two discrete points on the volute cutoff separation point. A special interest was in the effect of inclining either the cutoff or the impeller blades as an effective way to phase shift the pressure and thus the acoustic radiation. In summary, an increase in the blade number results in both aerodynamic and acoustic benefits. Regarding the volute cutoff, employing stepped geometries in the spanwise direction, the tonal noise was reduced due to destructive phase shifts and thus interference effects.

2. MATERIALS AND METHODS

To correlate the local aerodynamic quantities at the volute cutoff with the acoustic far-field radiation, an extensive experimental setup is required. Various test specimens were manufactured and tested while special care was taken in terms of detailed and accurate data processing and signal analysis.

2.1 Experimental Test Rig

The experimental test rig is situated in a semi-anechoic room at *TH Nürnberg Georg Simon Ohm* with a low-pressure centrifugal fan installed from the adjacent room, providing the pressure side flow without potential disturbances of the suction side and the electric motor.

The static pressure of the centrifugal fan is measured inside the duct at the fan inlet. On the pressure side, the static pressure is measured inside the anechoic room, where the dynamic pressure can be considered to be zero. In consequence, the fan static pressure rise of the fan is determined by the pressure difference on the suction and pressure side, corrected by the dynamic component at the inlet.

$$\Delta p_s = p_{s,inlet} - p_{s,outlet} - p_{dyn,inlet} \quad (1)$$

The flow rate is measured using pitot-static tubes at the nozzle exit prior to entering the centrifugal fan assembly. The flow rate, corresponding to the measured dynamic pressures at the duct outlet at midspan, is calibrated through detailed operational test increment measurements in preliminary experiments. The rotational speed is determined via a Sick WL24 optical sensor, whereas throttling takes place through automated flaps downstream of the settling section as can be seen in Figure 1.

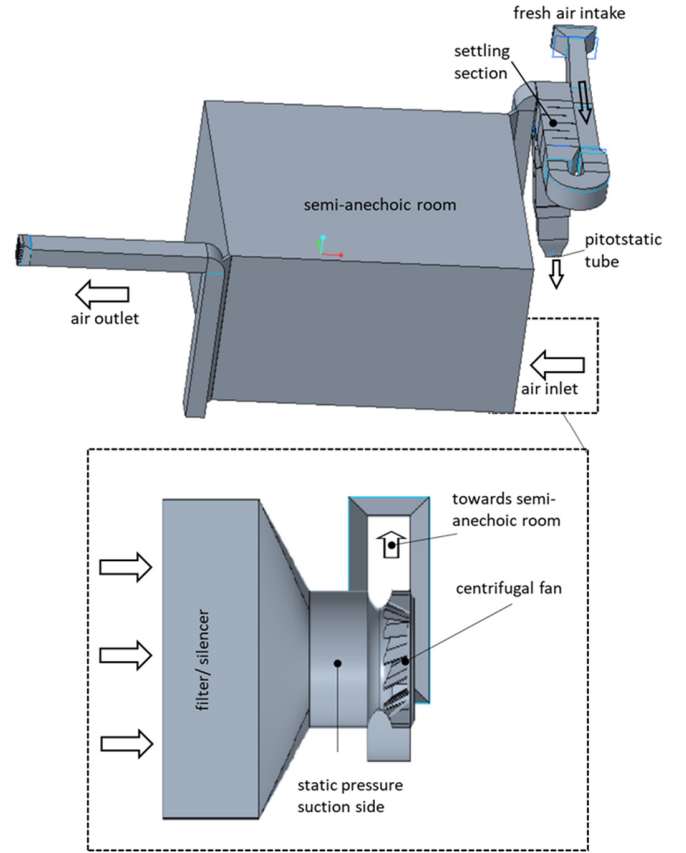


FIGURE 1: SCHEMATIC OF TEST FACILITY AND INSTALLED CENTRIFUGAL FAN.

To assess the aerodynamic and aeroacoustic performance of the prototypes, several key parameters were established. The aerodynamic characteristics were defined using the flow coefficient (Eq. 2) and pressure coefficient (Eq. 3), which provide a non-dimensional representation of the flow rate and total pressure rise, respectively. This approach allows for direct comparisons, regardless of impeller diameter and/or rotational speed.

$$\varphi = \frac{\dot{Q}}{U_{rot} \cdot A_{imp}} \quad (2)$$

$$\psi_T = \frac{\Delta p_T / \rho}{U_{rot}^2 / 2} \quad (3)$$

The centrifugal fan under investigation is a commercially used centrifugal fan for ventilation purposes as shown in Fig. 2. Hence, the provided static pressure rise is of limited quantity but high efficiency. The impeller width covers approximately 40% of the casing outlet span, and the minimum distance between the fan impeller and volute cutoff is 31 mm. The large distance is expected to affect the radiated noise from the volute cutoff, since the aerodynamic pressure magnitudes from the impeller blade trailing edges can interact with the mean flow before impinging on the cutoff geometry. Moreover, at off-design conditions, the

larger distance between the impeller and cutoff facilitates a smooth development of the backflow region at reduced interaction with the geometry.

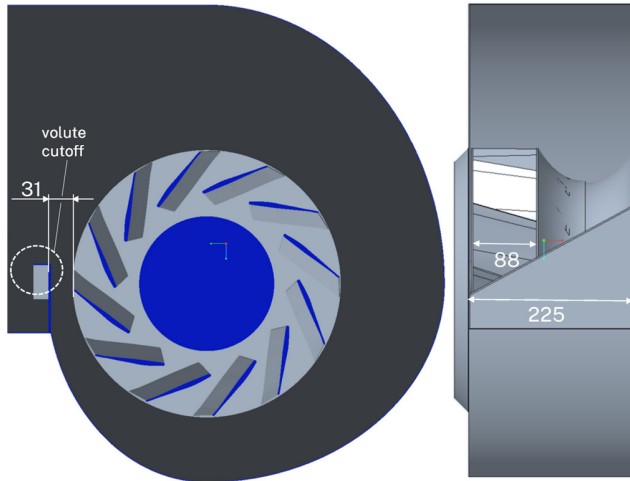


FIGURE 2: SIDE VIEW AND FRONT VIEW OF INVESTIGATED 12-BLADED CENTRIFUGAL FAN.

2.2 Sensors and Data Acquisition

Analyzing the acoustic and aerodynamic signatures in the near-field and the far-field and assigning relevant parts to the volute cutoff requires close-meshed monitoring of these quantities through experimental methods. As specified by Möser and Neise [10], a feasible method to gather information on the unsteady pressure fluctuations on a solid surface is the application of pressure tapping sensors (Fig. 3). These sensors consist of ¼” Roga RG-50 condenser microphones, connected through coupling units with cannula tubes. These tubes are flush-mounted to the rigid surface of the volute cutoff to communicate with the inner pressure field. The microphone is electrically decoupled from the metal cannula tube through the rapid-prototyped Polylactide coupling units. A minimum cannula length ensures a minimum locked-in air volume and an optimum transfer function with minimum damping effects. The first cannula duct mode is well above the human hearing range. Pressure equalization is maintained by connecting the compensation bore to the internal pressure field.

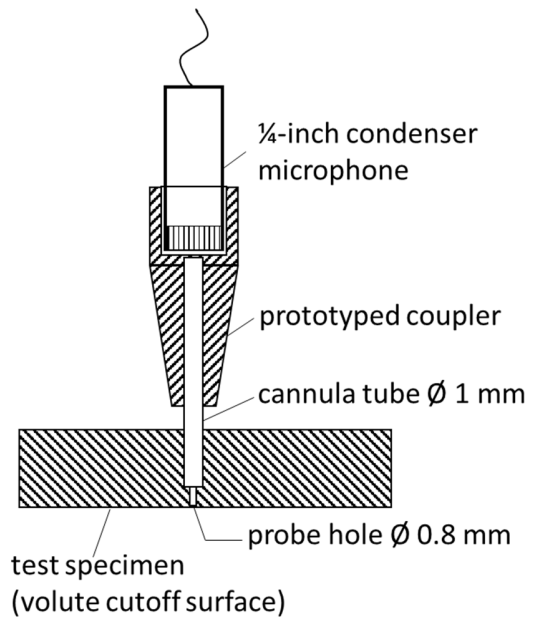


FIGURE 3: DESIGN OF A PRESSURE TAPPING SENSOR FOR THE UNSTEADY NEAR-FIELD STATIC PRESSURE FLUCTUATIONS ACCORDING TO MÖSER/ NEISE [10].

Four pressure tapping sensors are employed to monitor the unsteady pressure fluctuations at the volute cutoff in close vicinity to the impeller. The signals are sampled at 22,050 Hz and blocksize 22,050, yielding a spectral resolution of $\Delta f = 1$ Hz. Taking 134 spectral averages and Hanning windowing at 66% overlap results in stable and reliable signals at a total measurement duration of 45s. Furthermore, another 17 locations are identified along the volute cutoff to gather information on the mean static pressure distribution through $\varnothing 0.8$ mm cannula tubes, connected via pneumatic tubes. For doing so, a 24-channel SVM Tec PSC pressure scanner is employed at a sampling rate $SR = 10$ Hz, taking 450 averages. Figure 4 gives an overview of the distribution of the sensors along the cutoff geometry.

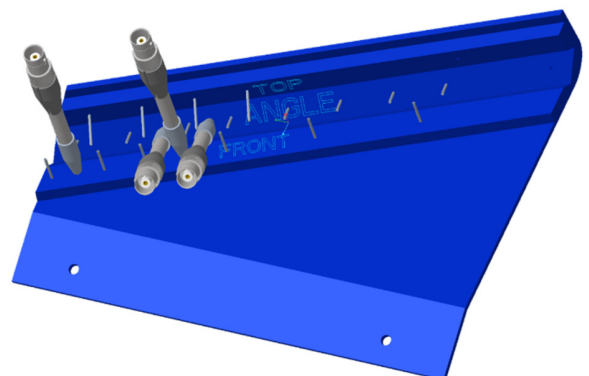


FIGURE 4: EXEMPLARY VOLUTE CUTOFF SECTION WITH 4 INSTALLED UNSTEADY PRESSURE TAPPING POINTS AND MEAN STATIC PRESSURE TAPPING POINTS.

The acoustic far-field is monitored via four ½" PCB-378B02 free-field microphones at an equal sampling and analyzing strategy as the near-field unsteady pressure tapping sensors. Three microphones are located at a radius of $R = 1.5$ m from the volute cutoff at the fan impeller mid-span on the same horizontal level, covering an azimuth distance of 120 deg relative to the focal point (Fig. 5). The remaining microphone shows a vertical displacement of $H = 0.75$ m, located normal to the volute cutoff.

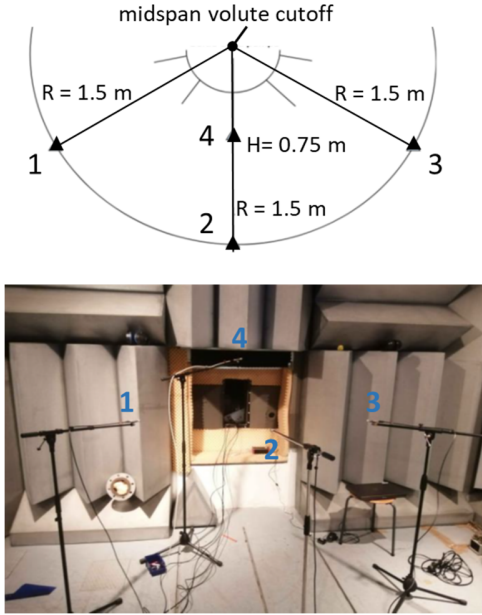


FIGURE 5: OUTFLOW SECTION OF CENTRIFUGAL FAN AND FAR-FIELD MICROPHONE POSITIONING.

Regarding aeroacoustic characteristics, it is important to distinguish between time and spectral domains. While the former provides information on total performance within a spectral range of $25 \text{ Hz} \leq f \leq 12,000 \text{ Hz}$, the latter gives detailed insights into dominant components and allows conclusions about potential underlying source mechanisms. Eq. 4 specifies the sound pressure level (SPL) for the far-field microphones, and Eq. 5 defines the local wall pressure level (WPL) of the unsteady pressure tapping points in the near-field at the volute cutoff.

$$\text{SPL} = 10 \cdot \log_{10} \left(\frac{p_{RMS}^2}{p_0^2} \right), p_0 = 2 \cdot 10^{-5} \text{ Pa} \quad (4)$$

$$\text{WPL} = 10 \cdot \log_{10} \left(\frac{p_{RMS}^2}{p_0^2} \right), p_0 = 1 \cdot 10^{-6} \text{ Pa} \quad (5)$$

To analyse the similarity of two given signals, correlation approaches in both the time and the spectral domain can be used. Separating similarity in terms of spectral components motivates the latter, where the coherence γ^2 (Eq. 6) is defined as the cross-spectral density of the input signals, normalised by the spectral

densities. Spectral components that exist in both signals are reinforced compared to those, present in only one of the signals.

$$\gamma^2(\omega) = \frac{G_{12}(\omega) \cdot G_{12}^*(\omega)}{G_{11}(\omega) \cdot G_{22}(\omega)} \quad (6)$$

2.3 Specimen & Prototypes

As outlined in Section 2.2, the volute cutoff is equipped with pressure tapping points for the steady and unsteady static pressure. Four different geometries of the volute cutoff are defined and manufactured via rapid prototyping. After preparation of the pressure tapping points, the centrifugal fan can operate with an open exhaust towards the semi-anechoic room (Fig. 6), the installed sensors being in the wind shadow of the cutoff, hence affecting neither the aerodynamic performance nor the acoustic radiation.

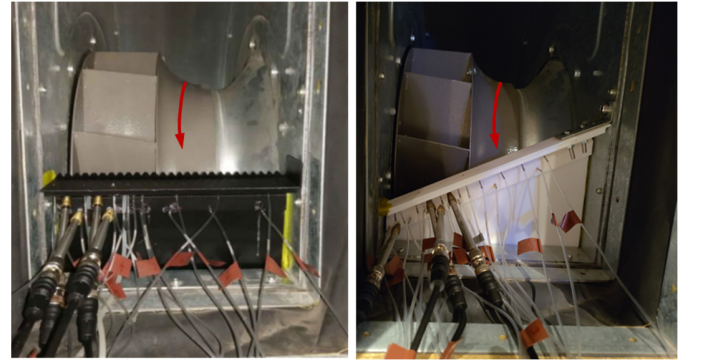


FIGURE 6: INSTALLED VOLUTE CUTOFF PROTOTYPES INCLUDING PRESSURE TAPPING SENSORS.

Four prototypes are tested in a preliminary study as can be seen in Figure 7. First, a straight cutoff design serves as the baseline reference case. Second, a cutoff equipped with riblets, distributed in the spanwise direction, where the critical height of $H = 3 \text{ mm}$ is estimated to resemble the height of the boundary layer, thus directing the flow and preventing spanwise mitigation of separated flow regimes. As a third sample, the cutoff is equipped with spikes to serve as aerodynamic turbulators, re-energising the boundary layer with the fluid of the free stream. Last, the fourth sample features a wavy contour of the cutoff tip, showing some similarity to sinusoidal leading-edge serrations even though of lower fidelity.

The distribution of the pressure tapping points shown in Figure 7 highlights the static pressure measurements (white) as well as the measurement location of the unsteady pressure (red), where the latter concentrates on the spanwise extension of the impeller relative to the volute cutoff.

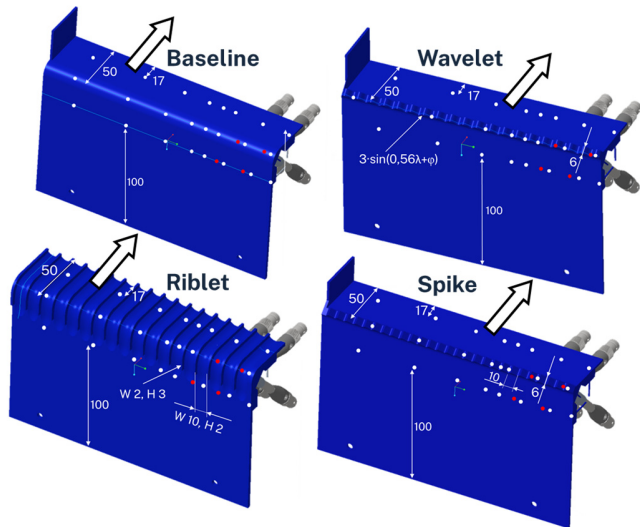


FIGURE 7: SPECIMEN OF INVESTIGATED CUTOFF DESIGNS. STATIC (WHITE) AND UNSTEADY (RED) PRESSURE TAPPING POINTS.

The aim of the current study is to assess the aeroacoustic potential of the volute cutoff design as well as the relation between near-field pressure information and far-field acoustic radiation. Naturally, various other and more detailed designs of the volute cutoffs are possible and meaningful. To date, the focus lies on obtaining significant differences between the single specimen, allowing to validate and refine the methodology.

3. RESULTS AND DISCUSSION

The overall aerodynamic performance is monitored simultaneously with the acoustic far-field radiation as well as the static and unsteady pressure distribution at the volute cutoff. Since the aeroacoustic dependencies are expected to be a function of the operation point, the entire characteristic curve of the centrifugal fan is evaluated.

3.1 Aerodynamic Results

In the first step, the defined setup consisting of the centrifugal fan, the anechoic chamber as well as the duct system is modelled numerically via ANSYS CFX. A steady state approach for the entire characteristic curve provides first insights into the overall flow behavior. As seen from the overview in Fig. 8, the primary region of high velocity is the fan exhaust, where the flow closer to the walls of the semi-anechoic room is of negligible magnitudes. This validates the approach to measure the static pressure inside the anechoic room while disregarding potential dynamic components, as described via ISO 5801 [11].

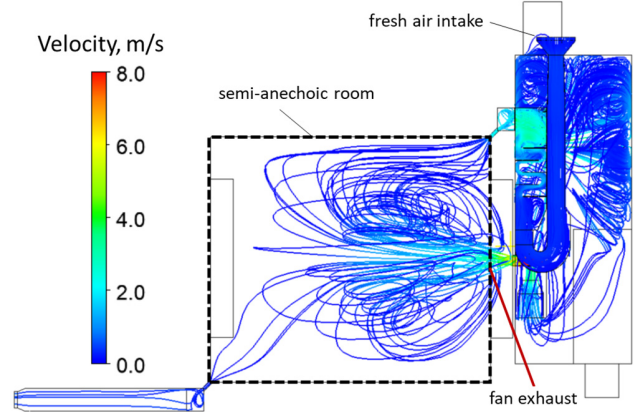


FIGURE 8: 3D VELOCITY STREAMLINES THROUGH THE TEST FACILITY.

Zooming into the fan exhaust at the midspan reveals the interaction of the impeller potential field with the volute cutoff in Figure 9, separating the flow between the spiral casing and the outflow duct. Depending on the spanwise flow field across the impeller and the cutoff, a highly three-dimensional pressure distribution is expected. Moreover, the local separation point at the cutoff is expected to vary as a function of the operation point.

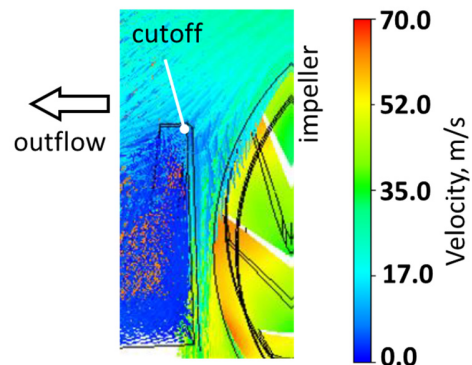


FIGURE 9: EXEMPLARY SNAPSHOT OF IMPELLER-CUTOFF INTERACTION.

As described previously, the characteristic curve of the fan is sampled at 10 discrete locations, while near-field information on the static and unsteady pressure as well as the far-field noise radiation and the global aerodynamic performance is gathered. Figure 10 shows the aerodynamic characteristic curves at three discrete rotational speeds $n = 800 \text{ min}^{-1}$, 1200 min^{-1} and 1585 min^{-1} , based on experimental measurements as well as the numerical model. Especially at low fan speed, the fit is of good quality, whereas more severe deviations are observed for higher speeds. This can mainly be assigned to the primary and secondary characteristics of the numerically obtained characteristic curves at high speeds, absent during the experiments. Since the internal resistance of the system prevents

the investigated fan from experimentally operating at maximum flow rates, the overload region is characterized by numerical results only.

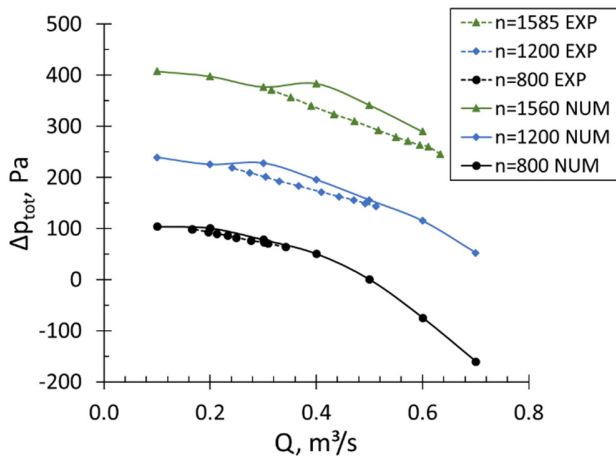


FIGURE 10: FAN CHARACTERISTIC CURVES AT VARYING SPEED: COMPARISON OF EXPERIMENTAL AND NUMERICAL RESULTS.

The aerodynamic results are normalized through the flow coefficient ϕ (Eq. 2) and pressure coefficient ψ (Eq. 3), respectively. Given that the machines are operating at similar physical boundary conditions, these curves are independent of fan speed, fan diameter and fluid density. Figure 11 shows an experimental comparison of the non-dimensional characteristic curves for the same fan with four different volute cutoff designs as outlined in Figure 7. Especially at part-load conditions with low flow rates and high inflow angles of the flow relative to the fan blades, the cutoff design tends to significantly affect the overall performance.

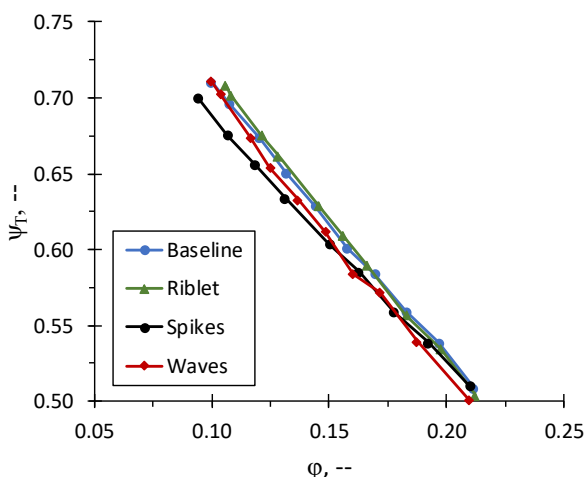


FIGURE 11: NON-DIMENSIONAL CHARACTERISTIC CURVES WHILE VARYING THE VOLUTE CUTOFF SPECIMEN.

A volute cutoff, equipped with riblets performs best in comparison to the spiked prototype, showing a reduced total pressure rise. At part-load conditions the flow separation point migrates downstream of the cutoff tip, establishing local backflow regimes. The tested riblet-cutoff is assumed to canalize these backflow phenomena as well as to limit the spanwise extensions of local unsteadiness.

To examine the local pressure distribution along the cutoff, Figure 12 provides an overview of 10 discrete operation points along the characteristic curve for the baseline reference case. The total spanwise extension of the cutoff is 225 mm, where the impeller serves as the counterpart for the first 88 mm (pressure tapping points 1 – 5, Fig. 12) in a distance of ≥ 31 mm only (compare Fig. 2). As can be seen in Figure 12, the distribution of the static pressure shows a strong dependency on both the spanwise position as well as the streamwise location. Upstream the cutoff tip (Fig 12, top), static pressures are low to negative in front of the projected impeller, clearly scaling with the operation point. This can be assigned to a local backflow region, reversing to the main flow direction and becoming stronger in a spanwise direction and with increasing resistance of the system or at reducing flow coefficients ϕ , respectively.

At the cutoff tip (Fig. 12 centre), however, the picture changes and the static pressure gradually increases as is also true for the upstream location in Figure 12 (bottom). For the latter, the local static pressure increases with reducing flow coefficient ϕ or total pressure increase along the characteristic curve as is seen in Figure 11. The left-skewed distribution of the pressure principally is well known for centrifugal fans of high flow rates and thus a deep spanwise casing. Moreover, it is expected to be reinforced by the inclination of the impeller blade trailing edges.

Extending the analysis of the static pressure towards different cutoff designs results in Figure 13 for three characteristic operation points along the characteristic curve at $\phi = 0.120$, $\phi = 0.158$ and $\phi = 0.197$. In general, the spiked cutoff design follows the pressure distribution of the baseline reference configuration. Qualitatively, the same is true for the wavy cutoff design even though the differences are of a different magnitude. This serves as an argument that these design features do not alter the general flow mechanisms to a significant degree. On the other hand, they might have an impact on the local noise generation and radiation. For the riblet cutoff design, however, a different pattern is observed, being of almost reverse character. Low static pressures are observed downstream of the cutoff tip and a gradual increase in the spanwise direction upstream of the cutoff. Both, the congruent pattern of the spiked cutoff and the deviating pattern of the riblet configuration cannot be assigned to the general aerodynamic performance as discussed in Figure 11. They rather serve as local indicators.

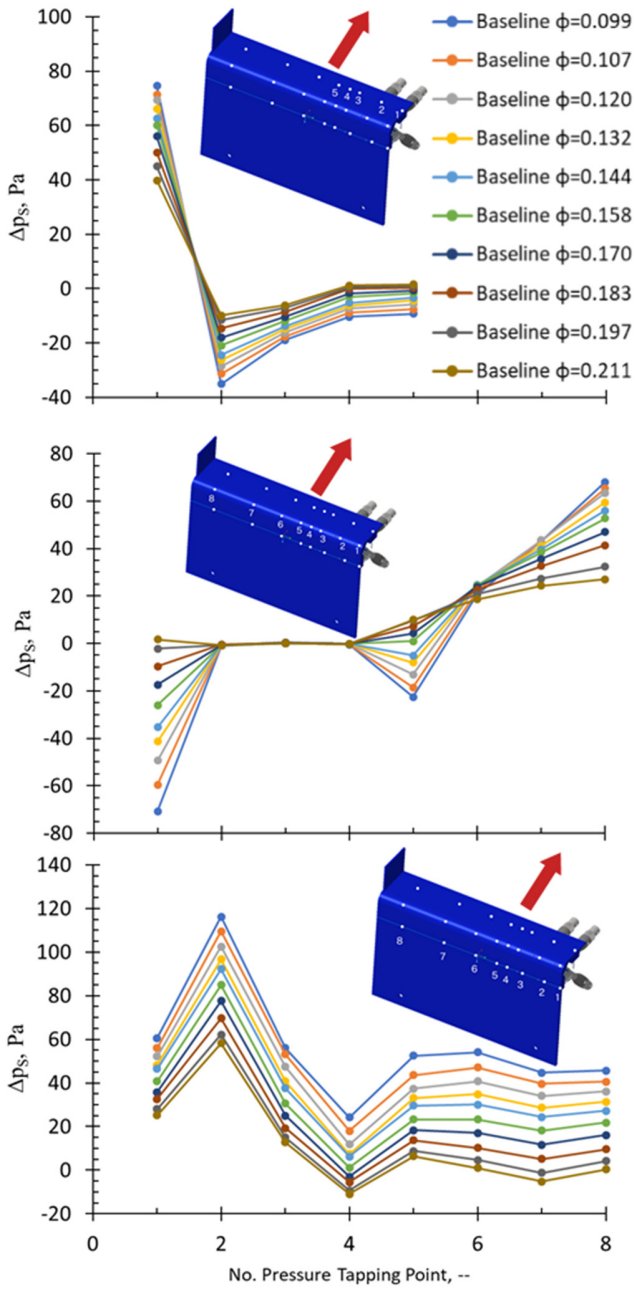


FIGURE 12: MEDIAN STATIC PRESSURE ALONG THE CUTOFF SPAN DOWNSTREAM THE CUTOFF TIP (TOP), AT CUTOFF TIP (CENTRE) AND UPSTREAM THE CUTOFF TIP (BOTTOM) FOR THE BASELINE REFERENCE.

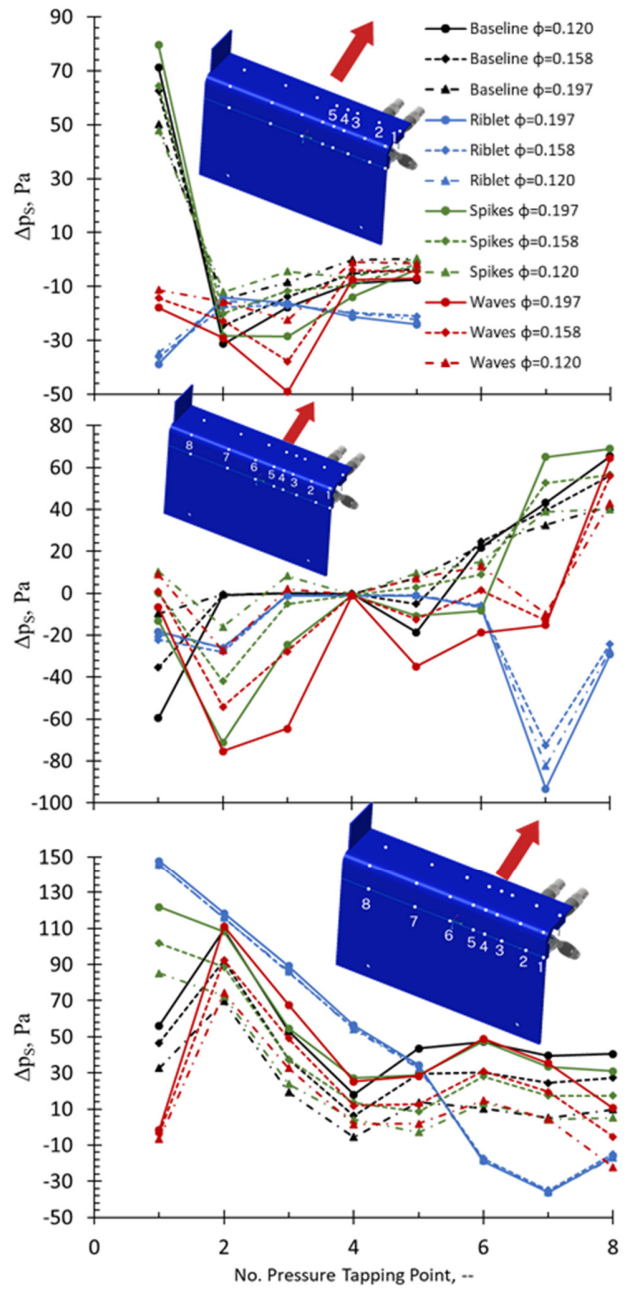


FIGURE 13: MEDIAN STATIC PRESSURE ALONG THE CUTOFF SPAN DOWNSTREAM THE CUTOFF TIP (TOP), AT CUTOFF TIP (CENTRE) AND UPSTREAM THE CUTOFF TIP (BOTTOM) FOR THE TESTED FOUR SPECIMEN AT THREE CHARACTERISTIC OPERATION POINTS.

3.1 Aeroacoustic Results

The aeroacoustic measurements are performed at fan speed $n = 1100 \text{ min}^{-1}$ along the full characteristic curve. The overall sound pressure level (Eq. 4) is determined as an average of the four installed $\frac{1}{2}$ " far-field microphones, incorporating directivity effects of the acoustic radiation. Figure 13 indicates a total margin of $\Delta\text{SPL} \approx 2 \text{ dB}$ along the characteristic curve. Comparing the tested cutoff designs shows the baseline reference case as well as the wavy cutoff to perform in a highly similar manner, as it was also the case for the total aerodynamic performance (Fig. 11). However, the spiked cutoff shows a poor performance in terms of acoustic far-field radiation in line with the aerodynamic performance. The riblets constantly show a noise reduction with an offset of $\Delta\text{SPL} \approx 1.0 \text{ dB}$, associated with a slight increase in total pressure as discussed in Figure 11.

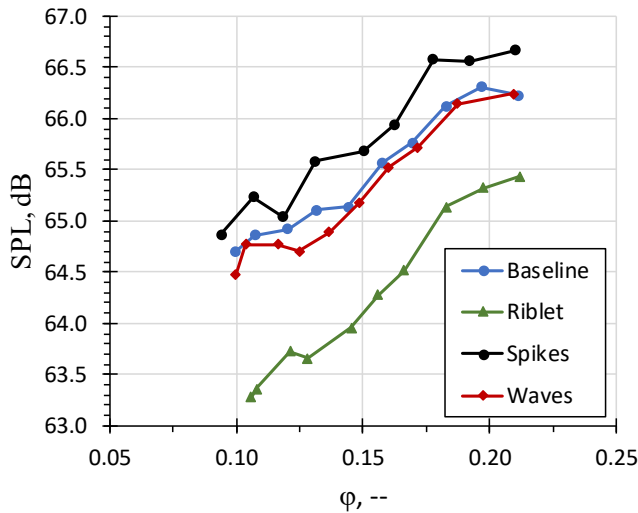


FIGURE 13: AVERAGED OVERALL FAR-FIELD SOUND PRESSURE LEVEL ALONG FAN CHARACTERISTIC CURVES, FEATURING FOUR TESTED VOLUTE CUTOFF DESIGNS.

Relating to the near-field information, Figure 14 shows the wall pressure level according to Equation 5 for the four installed unsteady pressure tapping points on the surface of the volute cutoff. As can be seen, the total levels depend on the installation position of the pressure tapping point, not reflecting the far-field ranking of the tested cutoff designs. The WPL sum levels tend to increase in the spanwise direction from the casing wall towards the center flow (Fig. 14 1→2, 3→4) as well as upstream towards the volute cutoff tip (Fig. 14 1→3, 2→4). For the pressure tapping points upstream of the cutoff tip, the obtained levels are in the same magnitude range, where the baseline reference and the riblets show the highest levels. For the cutoff tip, however, the picture changes, showing a clear differentiation between the single-tested cutoff designs. POS3, in close vicinity to the casing wall, shows a deviating behavior, where the wavy cutoff design shows the maximum level and the riblets minimum levels, in contrast to previous observations.

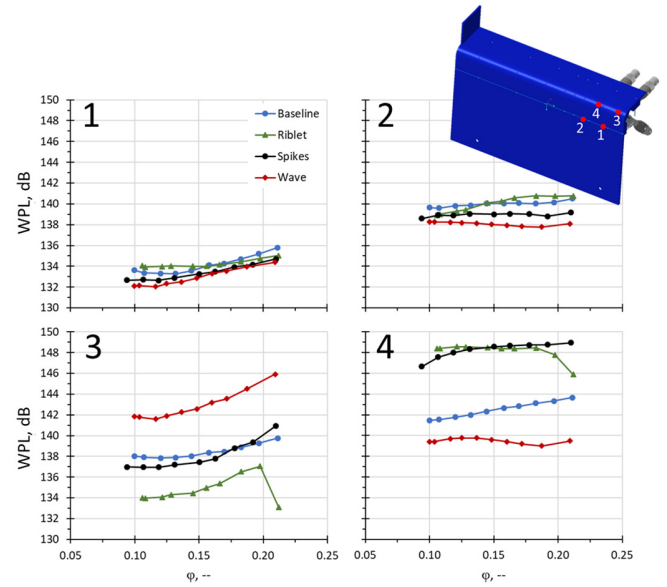


FIGURE 14: NEAR-FIELD WALL PRESSURE LEVEL AT FOUR DISCRETE LOCATIONS AT VOLUTE CUTOFF (FIG. 7) FOR THE TESTED CUTOFF DESIGNS.

3.1 Spectral Results

The spectral composition in Figure 15 for the far-field noise as well as in Figure 16 for the near-field unsteady pressure fluctuations allow for a more detailed view of the underlying mechanisms. Figure 15 clearly shows the fundamental rotational frequency at 18.3 Hz, the blade passing frequency at 221 Hz and the second harmonic in the far-field to dominate the tonal and discrete characteristics of the spectrum. In this regard, no significant differences are observed between the single cutoff designs. However, for the riblets a broadband noise reduction predominantly at $f < f_{\text{BPF}}$, but generally existing up to $f = 5 \text{ kHz}$, becomes evident. This pattern does not change with the operation point of the fan but remains on a relatively constant level.

Unlike the overall trends of the unsteady wall-pressure levels in Figure 14, the spectral components of the pressure fluctuations show a variation in amplitudes but not in composition. Therefore, they are averaged for brevity as displayed in Figure 16. In general, the primary fluctuations concentrate on a spectral range up to $f \leq 1500 \text{ Hz}$. For higher frequencies, a strong reduction of the fluctuation magnitudes is evident. As for the far-field, common discrete components are the fundamental frequency at $f = 18.3 \text{ Hz}$ as well as the blade passing frequencies and their harmonics ($n \cdot 221 \text{ Hz}$). At part-load, the baseline and the riblets perform at low magnitudes for high frequencies, whereas at lower frequencies the riblets always show maximum amplitudes. The picture changes towards overload conditions, where maximum fluctuations are observed for the riblet case across all frequencies. In summary, the baseline reference case shows minimum fluctuation levels across the different operation conditions.

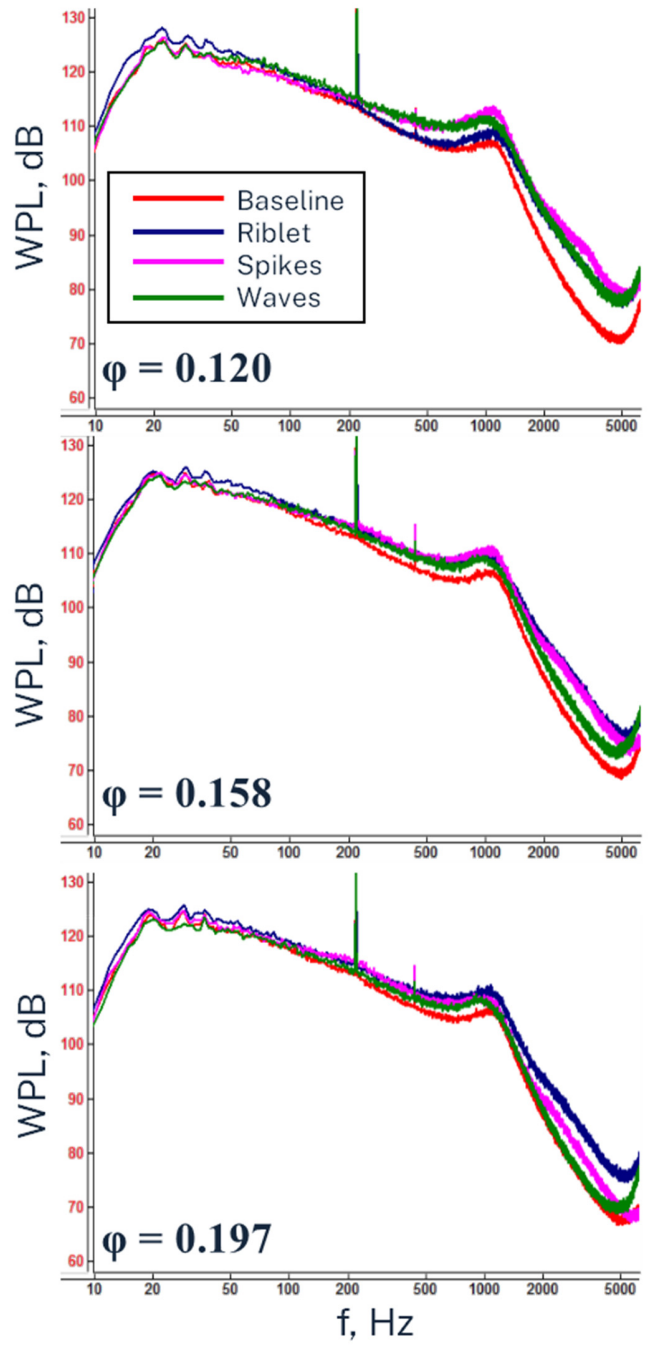
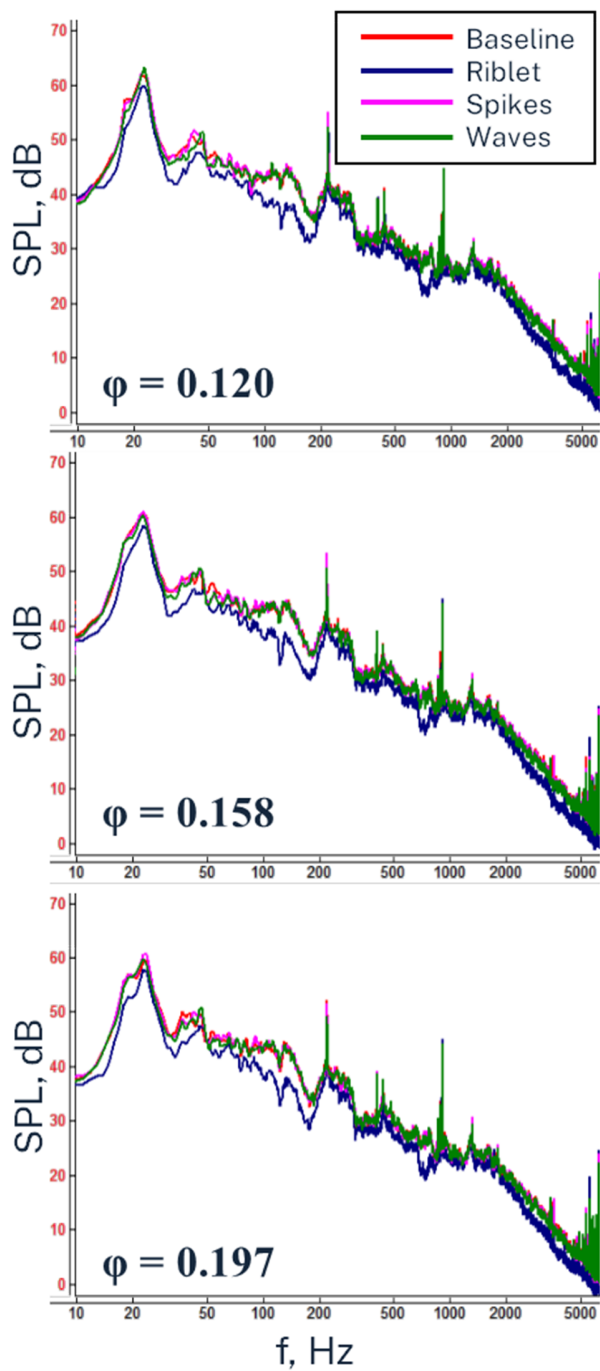


FIGURE 15: EXEMPLARY AVERAGED FAR-FIELD SPECTRA AT PART-LOAD (TOP), DESIGN (CENTRE) AND OVERLOAD CONDITIONS (BOTTOM) OF THE FAN FOR THE TESTED VOUTE CUTOFF DESIGNS.

FIGURE 16: EXEMPLARY AVERAGED NEAR-FIELD SPECTRA AT PART-LOAD (TOP), DESIGN (CENTRE) AND OVERLOAD CONDITIONS (BOTTOM) OF THE FAN FOR THE TESTED VOUTE CUTOFF DESIGNS.

Comparing Figures 15 and 16 indicates the discrepancy between local wall pressure fluctuation and far-field radiation, where low near-field magnitudes do not necessarily result in low noise radiation. Effects such as local radiation angles, directivity, decorrelation along swept surfaces and others are expected to play a key role in determining the transfer function between near-field and far-field. As a first step towards the link between these signals, an identification of common spectral components is necessary. As Figure 17 indicates, common parts between the wall pressure fluctuations and the far field noise are already visible such as the blade passing frequency and the fundamental rotational frequency at $f = 18.3$ Hz

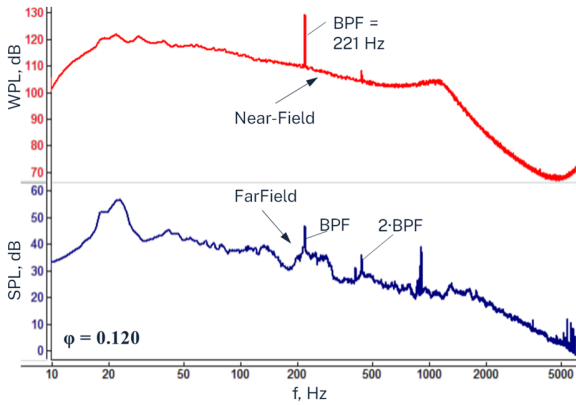


FIGURE 17: CONTRASTING JUXTAPOSITION OF FAR-FIELD (TOP) AND NEAR-FIELD SPECTRA (BOTTOM) AT PART-LOAD.

Quantification of common spectral parts between the near-field pressure tapping points and the far-field noise radiation takes place via defining the coherence γ^2 (Eq. 6), a spectral determination of common signal parts. Figure 18 shows maximum coherence in a spectral range up to $f \leq 2$ kHz, which can be confirmed by cross-correlation results as well as the circumstance of declining wall-pressure magnitudes at higher frequencies (Fig. 16). Coherent values close to 1 indicate a strong similarity between two independent signals and hence between the wall-pressure fluctuations at the volute cutoff and the far-field noise. Comparing the different volute cutoff specimens shows a dependency on spectral similarity. The baseline reference case, the spiked and the wavy prototypes show high coherence values up to maximum frequencies, whereas the riblets form a spectral cutoff at $f \leq \approx 700$ Hz. The riblets are considered to show decorrelation effects in terms of noise radiation and diffraction of noise, closely related to the geometric properties in terms of riblet height and width (Fig. 7). However, at this stage future studies are needed for further validation and optimization.

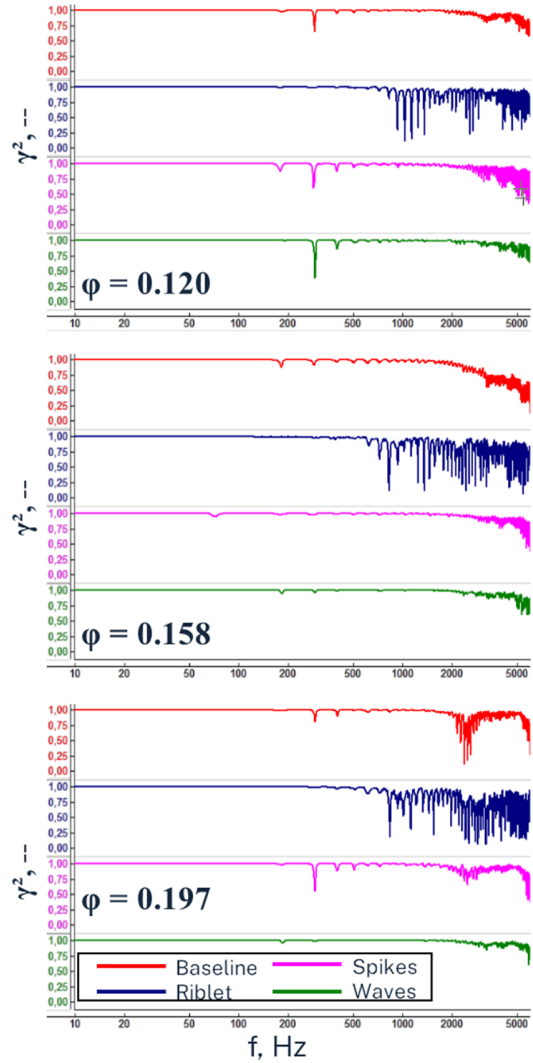


FIGURE 18: SPECTRAL COHERENCE BETWEEN FAR-FIELD AND NEAR-FIELD INFORMATION AT PART-LOAD (TOP), DESIGN (CENTRE) AND OVERLOAD CONDITIONS (BOTTOM) FOR THE TESTED VOLUTE CUTOFF DESIGNS.

4. CONCLUSION

An experimental study was conducted to gather the local steady and unsteady wall pressure fluctuations at different volute cutoff designs of a centrifugal low-pressure fan. The obtained signals are analyzed and correlated with the simultaneously measured acoustic far-field radiation to identify commonalities and are rated in terms of aerodynamic performance. The obtained results allow the paper to reach the following conclusions:

- The total aerodynamic performance is affected by the cutoff design, where the spiked volute cutoff destructively affects the total aerodynamic performance. Cutoff riblets are considered slightly favourable.

- Cutoff riblets show significantly lower noise radiation of $\Delta\text{SPL} \approx 1.0$ dB across the entire spectral range and at various operation points. This comes along with comparable or slightly improved aerodynamic performance.
- The observed maximum fluctuations at near-field locations do not necessarily result in maximum far-field levels as seen for the riblets, where local directivity, decorrelation and reflection properties are considered the key mechanisms.
- The volute cutoff shows strong similarities with the radiated far-field noise at frequencies $f \leq 2$ kHz, corresponding to an acoustic wavelength of $\lambda \approx 0.17$ m
- Coherent similarities of near-field and far-field information are affected by the volute cutoff design, where riblets show decorrelated effects for higher frequencies compared to the other test specimens.

Future work will need to focus on numerical validation and verification, including the local pressure distribution along the cutoff at varying operation points/ loads. For further experimental investigations, the use of high-pressure centrifugal fans with a low impeller to cutoff distance is considered meaningful to amplify the effects of interest.

ACKNOWLEDGEMENTS

The authors like to acknowledge and thank Mr. Antonio Tavares and Mr. Louison Hillairet, École Nationale Supérieure de Mécanique et d'aérotechnique ENSMA for their support in setting up the experimental environment and conducting the experiments.

REFERENCES

- [1] Eck, B. (2003) Ventilatoren, Entwurf und Betrieb der Radial-, Axial- und Querstromventilatoren, ISBN 978-3-642-55650-0, Springer Verlag, Berlin, Germany.
- [2] Neise, W. (1976) Noise Reduction in Centrifugal Fans: A Literature Survey, Journal of Sound and Vibration, Vol. 45(3): pp. 375-403
- [3] Bommers, L. (1997) Entwurfspolynome zur optimalen Auswahl und Bemessung von Industrieventilatoren radialer Bauart. V. Proceedings of Wissenschaftlich-Technische Konferenz Industrieventilatoren: pp. 39-51, Zakopane, Poland.
- [4] Patil, S. R., Chavan, S. T., Jadhav, N. S., Vadgeri, S. S. (2018) Effect of Volute Tongue Clearance Variation on Performance of Centrifugal Blower by Numerical and Experimental Analysis, ICMPC 2017 Materials Today: Proceedings, Vol. 5(2): pp. 3883–3894. DOI: 10.1016/j.matpr.2017.11.643
- [5] Dong, R., Chu, S., Katz, J. (1997) Effect of Modification to Tongue and Impeller Geometry on Unsteady Flow, Pressure Fluctuations, and Noise in a Centrifugal Pump, Journal of Turbomachinery, Vol. 119(3): pp. 506-515. DOI: 10.1115/1.2841152.
- [6] Zhang, J., Chu, W., Zhang, H., Wu, Y., Dong, X. (2016) Numerical and experimental investigations of the unsteady aerodynamics and aero-acoustics characteristics of a backward curved blade centrifugal fan, Applied Acoustics, Vol. 110: pp. 256-267. DOI: 10.1016/j.apacoust.2016.03.012
- [7] Manoochehr, D., Frank, S., Paschereit, C. O. (2015) Numerical and Experimental Study on the Tonal Noise Generation of a Radial Fan, Journal of Turbomachinery, Vol 137 (10): pp. 101005-1 – 101005-9. DOI: 10.1115/1.4030498
- [8] Biedermann, T.M., Moutamassik, Y., Kameier, F. (2022) Assessment of the Impeller/ Volute Relationship of Centrifugal Fans From an Aerodynamic and Aeroacoustic Perspective. Journal of Turbomachinery, Vol. 145(8). DOI: 10.1115/1.4062243
- [9] Darvish, M., S. Frank and C. O. Paschereit (2015). Numerical and Experimental Study on the Tonal Noise Generation of a Radial Fan. Journal of Turbomachinery, Vol. 137(10). DOI: 10.1115/1.4030498
- [10] Möser, M., Neise, W. (2009): Messtechnik der Akustik, pp. 651-652, Springer. DOI: 10.1007/978-3-540-68087-1
- [11] ISO (2017) Fans — Performance testing using standardized airways (ISO 5801:2017). ISO.